JOURNAL OF AIRCRAFT
Vol. 43, No. 5, September–October 2006

Effects of Freestream Turbulence on Wing-Tip Vortex Formation and Near Field

S. C. C. Bailey* and S. Tavoularis†
University of Ottawa, Ottawa, Ontario K1N 6N5, Canada
and
B. H. K. Lee‡
National Research Council of Canada, Ottawa, Ontario K1A 0R6, Canada

The formation and near-field development of a wing-tip vortex under the influence of freestream turbulence were examined using flow visualization and hot-wire anemometry. A low turbulence freestream as well as two cases of grid turbulence with different intensities and length scales were considered. In all cases, the tip vortex was found to form from three smaller vortices, but the turbulence in its core was found to intensify with increasing freestream turbulence. The vortex trajectory was found to be unaffected by freestream turbulence, but the wing wake that was rolling up around the vortex was observed to have a curvature that decreased as freestream turbulence increased. The mean axial velocity distribution in the low-turbulence case was neither jetlike nor wakelike but had an annular shape. Time-averaged velocity profiles measured in the turbulent freestream cases were wakelike, and it was inferred that the instantaneous profiles would be significantly affected by vortex meandering. Mean circumferential velocity distributions in the vortex core displayed self-similar developments in all cases examined. Finally, it was found that the apparent diffusion in the shear layer shed from the wing increased with increasing freestream turbulence.

Nomenclature

b	=	wing semispan
c	=	wing chord
c_L	=	section lift coefficient
M	=	turbulence grid mesh size
Re_c	=	Reynolds number based on chord
r	=	radial distance from mean vortex axis
$r_{\theta\,\max}$	=	radial distance of peak circumferential velocity
U_{eff}	=	effective cooling velocity as measured by single-sensor probe
U_p	=	peak excess or deficit of streamwise velocity with respect to local freestream velocity
U_x	=	velocity component in x direction
U_y	=	velocity component in y direction
U_z	=	velocity component in z direction
U_θ	=	circumferential velocity component with origin at mean vortex axis
$U_{\theta\,\max}$	=	peak value of circumferential velocity
U_0	=	local freestream velocity
U_∞	=	freestream velocity
u'_{eff}	=	standard deviation of effective cooling velocity
u'_x	=	standard deviation of velocity component in x direction
x	=	streamwise distance from wing quarter-chord location
x'	=	streamwise distance from wing leading edge in wing-aligned coordinates
y	=	spanwise distance from vortex center, positive orientation from wing root to tip
y_v	=	spanwise distance of mean vortex axis from wing tip
y'	=	spanwise distance from wing tip away from wing root in wing-aligned coordinates
z	=	distance in vertical direction from vortex center, positive orientation in direction of lift
z_v	=	vertical distance of mean vortex axis from wing quarter-chord location
z'	=	distance in vertical direction in wing-aligned coordinates
α	=	wing angle of attack
θ	=	angular coordinate measured from positive y to positive z
σ	=	standard deviation of random number generator
$\overline{\ }$	=	time averaging

Received 10 August 2005; revision received 8 November 2005; accepted for publication 8 November 2005.

*Graduate Student, Department of Mechanical Engineering. Student Member AIAA.
†Professor, Department of Mechanical Engineering.
‡Principal Research Officer, Institute for Aerospace Research. Associate Fellow AIAA.

Introduction

VORTICES generated at the tips of finite lifting surfaces, such as aircraft fixed wings, propellers, and helicopter rotors, are known to dominate the wake of the lifting surface. Airplane wing-tip vortices, appearing in pairs, can pose a hazard for other oncoming aircraft, especially in congested airport environments during takeoff and landing. On helicopters, vortices shed from one rotor blade can interfere with following blades, generating noise and vibrations. Although tip vortices are very persisting, their structure and stability can be affected by external influences, in particular by freestream turbulence, whether atmospheric or introduced by other nearby surfaces.

The flowfield downstream of a finite wing is quite complex. Differences in pressure along the span of a finite wing induce a spanwise component of velocity over the surface of the wing. At the tip, fluid from the pressure surface rolls up toward the suction surface, forming a discrete vortex that is convected downstream. At the trailing edge of the wing, the spanwise flow generates a spanwise shear layer, which is also convected downstream. At the same time, the boundary layers on the two surfaces merge into a wake, which has streamwise momentum deficit and coexists with the shear layer.

The formation process of a wing-tip vortex depends largely on the wing geometry. Planform shape affects the distribution of pressure on the wing and, thus, the spanwise flow. Boundary layers on the wing contain turbulence and vorticity, which are entrained in the vortex during rollup.[1] Depending on the shape of the wing tip, rollup of the main vortex may include the merging of multiple small

vortices forming from local separated shear layers.[2,3] Finally, additional corotating vortices, generated by part-span flaps and other discontinuities, could merge with the main vortex at some downstream distance from the tip.[4]

Downstream of the wing, the shear layer and the wing wake roll up in a spiral around the vortex. This rollup process continues until the shear layer vorticity has fully merged into the vortex vorticity through turbulent and molecular diffusion. The fully developed vortex has a core in which viscous effects dominate and the circumferential velocity increases linearly with radial distance from the vortex axis, as in rigid-body rotation. Outside the core, the circumferential velocity reaches a maximum at some radial distance and then gradually decreases.[1] Axisymmetric, linear stability analyses indicate that fluid rotation in the vortex core stabilizes the motion, obstructing the generation of turbulence[5,6] and causing boundary-layer turbulence entrained in the vortex during rollup to decay rapidly.[7]

In the initial stages of vortex formation, the pressure in the vortex core gradually decreases along the vortex axis, generating a favourable axial pressure gradient that accelerates the core fluid in the streamwise direction, possibly resulting in a jetlike core having an axial velocity surplus.[8] Farther downstream, viscous actions[9,10] decelerate the flow, tending to convert the core to wakelike, having a velocity deficit relative to the freestream. In either case, the axial velocity gradient introduces a possible mechanism of turbulence production in the core.[11] However, turbulence generated in this manner tends to reduce the axial velocity gradient through turbulent diffusion, thus weakening any additional production of turbulence.[12] While this takes place, the stabilizing action of the fluid rotation continually impedes radial motions, promoting turbulence decay. In consideration of these competing mechanisms, it becomes uncertain whether the vortex core will be laminar or turbulent.

Available experimental evidence regarding the existence of turbulence within the core is inconclusive, mainly due to interference caused by transverse motion of the vortex in the measurement plane. This motion, referred to in the literature as either vortex wandering[8,13] or meandering,[1,7] is described as long-wavelength, low-frequency motion of the vortex that can occur even in relatively low-turbulence intensity wind tunnels. Vortex wandering interferes with the measurement of vortex characteristics by fixed probes, having an effect similar to that of turbulent diffusion: Measured time-averaged radial profiles of mean velocity components and turbulent velocity moments tend to be smoother and spread over wider radial distances, compared to corresponding actual profiles. Additionally, lateral motion of the vortex past the measuring probe introduces apparent velocity fluctuations, especially within the core where the radial gradients of the velocity are large. These fluctuations may be difficult to distinguish from local turbulence and may even make a laminar vortex core appear as turbulent. In a detailed study in which they corrected their measurements for vortex wandering, Devenport et al.[8] concluded that the core of a wing-tip vortex generated in a low-turbulence wind tunnel was laminar.

Turbulence external to the vortex, such as turbulence in the freestream or in the spiral wake/shear layer, can conceivably have several effects on the vortex. First, freestream turbulence could possibly affect the formation and rollup of the vortex. Second, farther downstream, freestream turbulent eddies would introduce meandering of the vortex; when sufficiently strong and of sufficiently large scale, this meandering could cause instability and breakdown of the vortex. Finally, energetic external turbulent eddies could possibly penetrate the vortex core, resulting in vortex decay. Despite the interest in the interaction between a vortex and a turbulent freestream, there have been surprisingly few quantitative experimental studies of the effects of freestream turbulence on vortex formation and rollup.

Bandyopadhyay et al.[14] observed a significant increase in vortex meandering motion with increasing freestream turbulence and an intermittent exchange of core fluid with turbulent freestream fluid, suggesting that freestream eddies penetrate the vortex core. Three-dimensional simulations[12,15] identify the formation of secondary vortical structures surrounding the vortex as a possible mechanism causing vortex meandering and core penetration. These structures form by the rolling of freestream eddies around the vortex, which stretches them azimuthally and intensifies their vorticity. Adjacent eddies with nearly aligned vorticity directions merge, creating secondary pairs of structures with opposing vorticity. The velocity field induced by such a pair can strip vortical fluid from the core and introduce vortex meandering through bending waves in the vortex.[16] Holzäpfel et al.[15] also found that, in the presence of a highly energetic freestream, the eddies might not form secondary structures but instead tend to bend and distort the vortex, initiating large-scale vortex instability and breakup.

The objective of the present study is to investigate experimentally the effects of freestream turbulence on the vortex formation, rollup, and development in the near field within 10 chord lengths of the wing. Besides a low-turbulence case, used for comparisons, two freestream turbulent conditions were generated using grids upstream of the wing, and the resulting velocity fields were measured in six transverse planes downstream of the wing. The present paper is an account of time-averaged statistics, establishing a basis for future experimental refinement and for the testing of numerical simulations. Detailed studies of wandering effects on the apparent turbulent stresses in the vortex core are currently in progress and will hopefully be the topic of a future paper.

Experimental Facilities and Instrumentation

Experiments were conducted in an open-circuit, suction-type wind tunnel, having a test section with dimensions $0.6 \times 0.9 \times 3.7$ m^3 and equipped with an automated three-axis, streamlined traversing system with a step resolution of 0.005 mm. The wing used to generate the vortex was machined from a solid aluminium plate. It had a NACA 0012 profile, a square tip and a rectangular planform with a chord of $c = 177.8$ mm and a semispan of $b = 520.7$ mm, corresponding to an aspect ratio of 2.93. The wing was instrumented with arrays of pressure taps at the five spanwise stations $0.68b$, $0.83b$, $0.93b$, $0.95b$, and $0.96b$. Each array had one tap at the leading edge, nine taps on the suction surface, and eight taps on the pressure surface. A boundary-layer trip wire of diameter 0.58 mm was located at the 10% chord location on the suction surface to reduce sensitivity to initial conditions for the different cases considered. The wing was placed vertically along the tunnel centerline at a distance of 0.6 m from the end of the contraction. A circular end plate was fitted near the root, $0.18c$ away from the tunnel wall to minimize tunnel boundary-layer effects. The experimental setup is shown in Fig. 1.

Freestream turbulence was generated by square-mesh perforated plates (grids), inserted across the flow at the inlet of the test section. Two grids were used, both with a solidity of 0.44; the large grid had a mesh size of $M = 50.8$ mm, whereas the small grid had a mesh size of 25.4 mm. The freestream streamwise turbulence intensity, $u'_x/\bar{U}_x$, measured with the wing and the grids removed, was found to

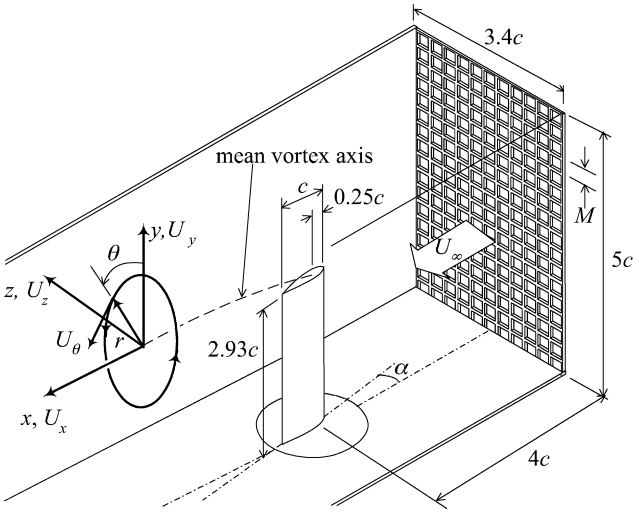

Fig. 1 Experimental setup.

be nearly uniform and less than 0.4% across the core of the tunnel. At the same streamwise cross section as the wing leading edge, the turbulence intensity was 5% for the large grid and 2.5% for the small grid, decaying to about 2% and 1%, respectively, at the end of the test section. The streamwise integral length scales of the freestream turbulence were 25 mm (large grid) and 17 mm (small grid) at the wing leading edge and 34 mm (large grid) and 23 mm (small grid) at the end of the test section.

A custom-built, four-sensor, modified Kovasznay-type hot-wire probe was used to measure the instantaneous, local velocity vector, both in magnitude and in direction. The sensors were made of platinum–10% rhodium and had diameters of 2.5 μm and lengths of 0.66 mm. The probe had a measurement volume of $0.68 \times 0.68 \times 0.46$ mm,^{3} and was mounted on a sting so that its tip was 0.38 m upstream of the automated traversing system to minimize interference. Freestream velocity was measured by a second hot-wire probe, having a single platinum–10% rhodium sensor, 5 μm in diameter and 2 mm long. This sensor was located 0.3 m upstream of the wing and 0.1 m away from the wall. The hot-wire probes were powered by constant temperature anemometer circuits (A.A. Lab. Systems, Ltd., Model AN-1003) and were recorded by a simultaneous sample-and-hold data acquisition system (United Electronic Industries PowerDaq Model PD2-MFS-8-300/16). All signals were low-pass filtered at a cutoff frequency of 8.2 kHz and digitized at a rate of 20 kHz. Ensemble-averaged statistics were calculated from samples with a length of 15 s, each segmented into 20 records of duration 0.5 s and separated from each other by intervals of 0.25 s.

All sensors were calibrated vs the streamwise velocity measured with a pitot tube/wall tap combination before and after each run. Velocity was determined from measured voltages using the lookup table data reduction technique described by Wittmer et al.,[17] which is capable of determining flow angles within an acceptance cone of approximately 30 deg. For cases for which the flow angle was found to be outside this cone, the velocity was determined using the method of Döbbeling et al.[18]

In a preliminary stage of the wind-tunnel investigation, oil-film flow visualization and single-wire hot-wire anemometry were used to investigate qualitatively the vortex formation process at $\alpha = 8$ deg and a freestream velocity of $U_\infty = 20$ m/s, corresponding to $Re_c = U_\infty c/\nu = 2.4 \times 10^5$. The flow visualization was performed using a suspension of copier toner in light machining oil. The sensor for the single-wire measurements was made of platinum-coated tungsten and had a diameter of 5 μm and a length of 2 mm. Single-sensor measurements were conducted at six transverse planes located at $x/c = 0.0, 0.25, 0.4, 0.55, 0.65$, and 0.75, for two freestream conditions corresponding to the unobstructed flow and a flow downstream of the large grid.

Measurements with the four-sensor probe were also performed at $Re_c = 2.4 \times 10^5$; however, the wing angle of attack was reduced to $\alpha = 5$ deg to ensure that flow angles remained within the probe's acceptance cone. The effective angle of attack, estimated using the general downwash blockage correction of Rae and Pope,[19] was 5.6 deg. The origin of the coordinate system (Fig. 1) was fixed at the tip of the wing, $0.25c$ from the leading edge, with its transverse location adjusted for each measurement plane to coincide with the center of the vortex. Measurements were conducted at six transverse planes, located at $x/c = 0.8$, 1.75, 3.75, 5.75, 7.75, and 9.75, for three freestream turbulence conditions, corresponding to the unobstructed flow, a flow downstream of the small grid, and a flow downstream of the large grid. In general, results at $x/c = 0.8$ are not included in this paper because the vortex core was not fully developed at this streamwise location and, also, flow angles approached the edge of the probe's acceptance cone.

Quantifying the uncertainty in curve fitting of calibration data and in converting measured cooling velocities to Cartesian velocity components is not a trivial task. Following Wittmer et al.,[17] uncertainties in the data reduction technique were estimated by comparing the Cartesian velocity components measured by the probe to those calculated from the calibration jet velocity and probe orientation as $\Delta\bar{U}_x/U_\infty \approx 0.2\%$, $\Delta\bar{U}_y/U_\infty \approx 0.5\%$, and $\Delta\bar{U}_z/U_\infty \approx 0.4\%$ for flow angles less than 20 deg and as $\Delta U_x/U_\infty \approx 0.6\%$, $\Delta U_y/U_\infty \approx 0.8\%$, and $\Delta U_z/U_\infty \approx 0.7\%$ for a flow angle of 30 deg. The streamwise position uncertainty was $\Delta x/c \approx 3\%$. The uncertainty in relative spatial position within a measurement plane due to the finite size of the probe was $\Delta y/c \approx \Delta z/c \approx 0.3\%$. The uncertainty in absolute spatial position (referenced to the wing), caused by reinsertions of the probe in the wind tunnel, was $\Delta y'/c \approx \Delta z'/c \approx \Delta y_v/c \approx \Delta z_v/c \approx 1\%$.

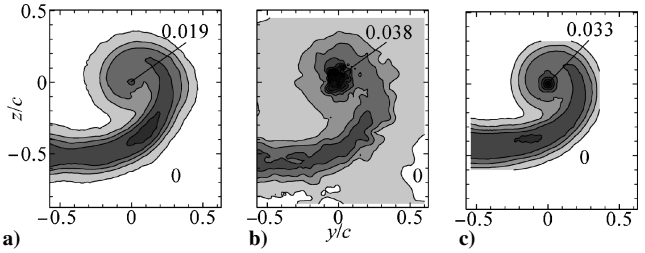

Fig. 2 Isocontours of standard deviation of streamwise velocity u'_x/U_∞ at $x/c = 9.75$: a) with $0.68 \times 0.68 \times 0.46^3$ four-wire probe, b) with $2.8 \times 2.8 \times 1.4$ mm^3, four-wire probe, and c) Devenport et al.[8] results.

A concern when using hot-wire probes is the possibility of flow distortion. Using flow visualization, Devenport et al.[8] found that a four-wire probe of nearly identical dimensions as those used in this study did not cause measurable disturbances within the vortex core. The presently measured intensity of the streamwise velocity fluctuations in the vortex core (Fig. 2a) was much lower than that in the Devenport et al. study at the same x/c and α but at different Re_c and aspect ratio (Fig. 2c), implying that probe-induced disturbances were negligible in the present case as well. The issue of possible probe disturbances was addressed early in this study, when measurements were taken with a larger four-wire probe, having a measurement volume with dimensions $2.8 \times 2.8 \times 1.4$ mm^3. Representative results with this probe, presented in Fig. 2b, show significantly stronger velocity fluctuations than those measured with the smaller probe. In Fig. 2, contour lines are spaced 0.004 apart.

In the present paper, no corrections for vortex wandering have been applied to the measurements. Instead, estimates of the wandering amplitude were made based on the correction method of Devenport et al.[8] This method uses a summation series to represent the measured profile and remove the effect of an estimated amount of wandering from the profile. The wandering estimate is then iteratively corrected until the estimated stresses at the vortex center match the measured stresses. This correction technique for point measurements was found to compare favorably with results from particle image velocimetry (PIV) studies.[20] When this process was used, it was estimated that the wandering amplitude was about 0.8 mm at the farthest downstream measuring plane for the unobstructed flow case. For this case, it has been estimated that wandering would have a negligible effect on mean circumferential velocity measurements, albeit a measurable one on the turbulent stresses in the core of the vortex. Application of this method did not produce any reliable corrections for the two grid turbulence cases.

In addition to the wind-tunnel measurements, a series of flow visualization experiments by dye injection was performed in a closed-circuit water tunnel, with test section dimensions of $0.6 \times 0.9 \times 3.7$ m. The water tunnel was equipped with two turbulence grids with mesh sizes and solidities identical to those used in the wind-tunnel studies. Dye was injected into the water tunnel at isokinetic conditions through two 1-mm-diam injectors, which could be moved throughout the test section to visualize different flow regions. The wing used in these experiments had a chord of $c = 177.8$ mm and a semispan of $b = 228.6$ mm, corresponding to an aspect ratio of about 1.3. A boundary-layer trip was also employed on this wing, which ensured that the flow over the suction surface was attached. (This was verified by flow visualization.) The water tunnel studies were conducted at a freestream velocity of $U_\infty = 0.16$ m/s, corresponding to a Reynolds number of $Re_c = 2.9 \times 10^4$ and an angle of attack of $\alpha = 5$ deg. In view of differences in wing aspect ratio and Reynolds number from the

wind-tunnel experiments, the water-tunnel results were used only for qualitative purposes, to assist in the understanding of the vortex formation process.

Results and Discussion

Vortex Formation

To characterize the vortex formation process and identify possible effects of freestream turbulence, single-sensor hot-wire measurements were performed at the wing tip and over the suction surface at $\alpha = 8$ deg and $Re_c = 2.4 \times 10^5$ for both the no-grid and large-grid cases. Single-sensor hot wires with a sensor axis normal to the probe axis measure an effective cooling velocity U_{eff}, defined as the equivalent flow velocity parallel to the probe axis that would produce the same sensor cooling as the actual flow velocity, and are unable to resolve the actual velocity magnitude and direction. Nevertheless, by comparison of single-sensor measurements downstream of the wing to four-wire measurements of the velocity vector, it has been found that the shapes of isocontours of the rms effective cooling velocity u'_{eff} matched fairly well the shapes of isocontours of the turbulent kinetic energy. Isocontours of u'_{eff}/U_∞ are presented in Figs. 3a and 3b, for the no-grid and large-grid cases, respectively. Both sets of contours presented maxima of u'_{eff}/U_∞ at approximately the same locations. At $x/c = 0.0$, two local maxima (peaks) were evident, one at the wing tip, A in Fig. 3, and another toward the suction surface near the tip, B in Fig. 3. In downstream measurement planes, the location of peak A moved toward the suction surface, rolling over the tip's edge somewhere between $x/c = 0.4$ and $x/c = 0.55$. Peak B, remained close to the suction surface in downstream planes, moving away from the tip until peak A rolled over to the suction surface, at which point it started to move toward the tip again. Peak A was wider than peak B in all planes and contained higher values of u'_{eff}/U_∞. At $x/c = 0.75$, the two peaks A and B appeared to have merged together. A smaller peak, C in Fig. 3, was also evident, appearing in the farthest downstream planes near the very tip of the wing.

The locations of the local peak values of u'_{eff}/U_∞ are indicated in Fig. 4 for both the no-grid and large-grid cases. In Fig. 4, the x, y, z coordinate system has been rotated by α to x', y', z' to align the coordinate system with the wing chord line. As can be observed in Fig. 4, the locations of peaks A, B, and C do not appear to be altered by the introduction of freestream turbulence.

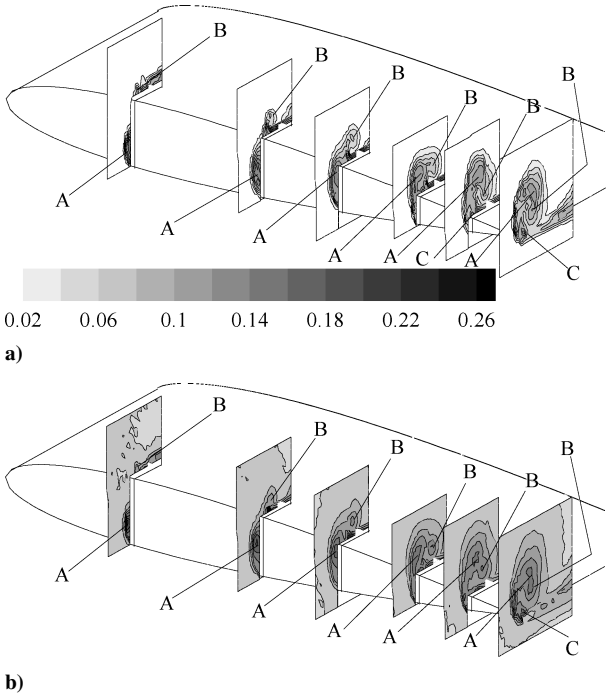

Fig. 3 Contours of u'_{eff}/U_∞ measured at $x/c = 0.0$, 0.25, 0.4, 0.55, 0.65 and 0.75 for a) no-grid case and b) large-grid case.

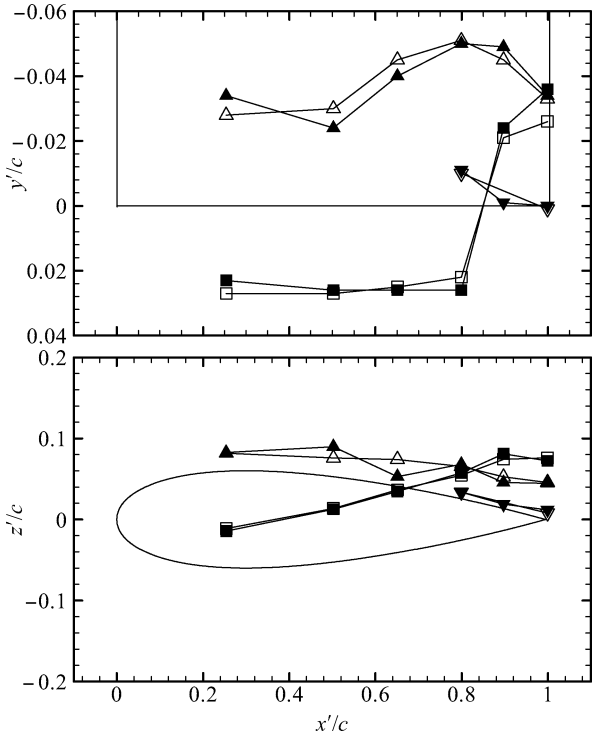

Fig. 4 Peak u'_{eff}/U_∞ locations for no-grid (solid symbols) and large-grid (hollow symbols) cases in wing-aligned coordinates: ■ and □, peak A; ▲ and △, peak B; and ▼and ▽, peak C.

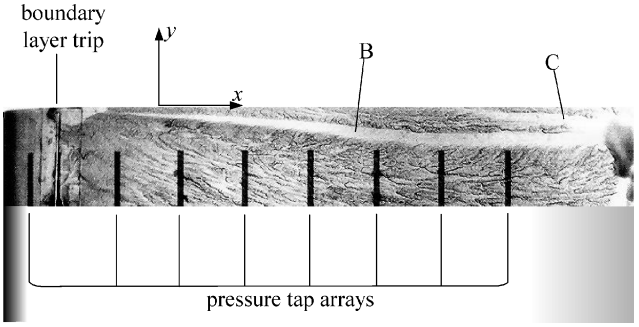

Fig. 5 Oil-film flow visualization with oil-free regions corresponding to signatures of vortices B and C on wing surface and locations of boundary-layer trip, pressure tap rows, and coordinate system origin.

Although the locations of the characteristic peaks were unaltered by freestream turbulence, larger u'_{eff}/U_∞ values were recorded for the large-grid case and the contours of u'_{eff}/U_∞ were wider, appearing more diffuse. If the vortex position were steady, this observation would indicate that freestream turbulence increased the turbulence inside the vortex during formation. However, in view of the steep local velocity gradients that could result in large measured values of u'_{eff}/U_∞ under even small-scale meandering, one needs additional evidence before making such a statement with any degree of confidence.

Oil-film surface flow visualizations were performed on the suction surface of the wing near the tip at $\alpha = 8$ deg and $Re_c = 2.4 \times 10^5$ for the no-grid and large-grid cases. A representative image for the no-grid case is shown in Fig. 5, with virtually identical patterns observed for the large-grid case. Two characteristic lines are evident as oil-free regions in Fig. 5, indicating high local wall shear stress. Comparison of the oil-film flow visualization and single-sensor measurements indicate that the high local wall shear stress corresponds to peaks B and C as indicated in Fig. 5.

To characterize the time-dependent aspects of the vortex formation process, flow visualization by dye injection was performed in the water tunnel at $Re_c = 2.9 \times 10^4$ and $\alpha = 5$ deg for the no-grid,

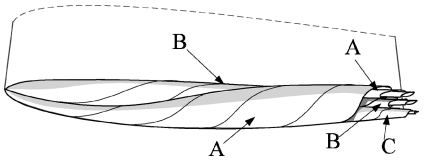

Fig. 6 Formation of discrete vortices based on observations using dye injection.

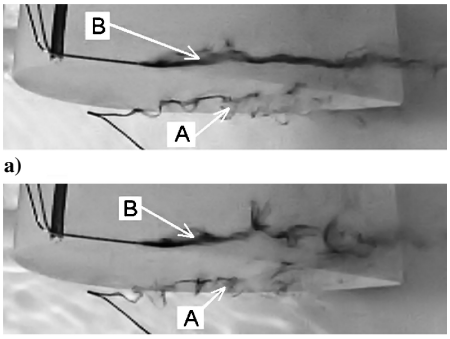

Fig. 7 Dye-injection images with vortices A and B for a) no-grid and b) large-grid cases.

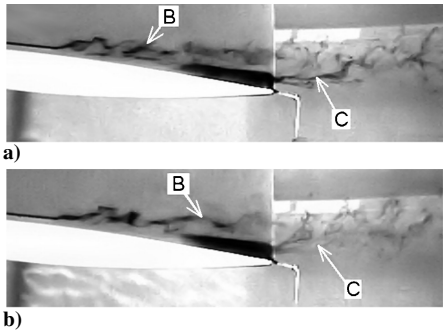

Fig. 8 Dye injection patterns with vortices B and C for a) no-grid and b) small-grid cases.

small-grid, and large-grid cases. Despite differences in Reynolds number, aspect ratio, and angle of attack between these experiments and the wind-tunnel studies, comparisons between patterns observed in the dye-injection images and those inferred from single-wire measurements showed strong qualitative similarities. The dye-injection flow visualization revealed that, in the initial formation phase, one could identify three distinct corotating vortices, shown in Fig. 6, that correspond to the characteristic peaks A, B and C in the contours of u'_{eff}/U_∞. Vortex A developed along the wing tip, as fluid from the pressure surface flowed around the tip edge. Vortex B developed along the suction surface, as fluid from the tip surface rolled up around the other edge of the tip. Finally, vortex C formed at the very tip of the trailing edge, as slow-moving fluid on the pressure surface rolled toward the suction surface near the tip of the trailing edge. Other experimental studies using flow visualization, velocity, and pressure measurements[2,3,21] have also identified the formation of multiple vortices, the number and arrangement of which varied with wing-tip geometry.

Based on observations of the rotation rate of the injected dye, vortices A and B appeared to be comparable in strength; however, vortex A was initially more turbulent, as evident from an increased rate of dye diffusion and increased fluctuation levels measured by the single-sensor probe. At approximately $x/c = 0.5$, vortex A rolled over to the suction surface and began to interact with vortex B. The interaction of the two vortices was turbulent and could not be observed in detail due to strong dye diffusion in both vortices.

All three vortices were noticeable in the three cases at different freestream turbulence levels, as shown in representative dye-injection images in Figs. 7 and 8. When the grids were placed upstream of the wing, dye injection showed that the formations and

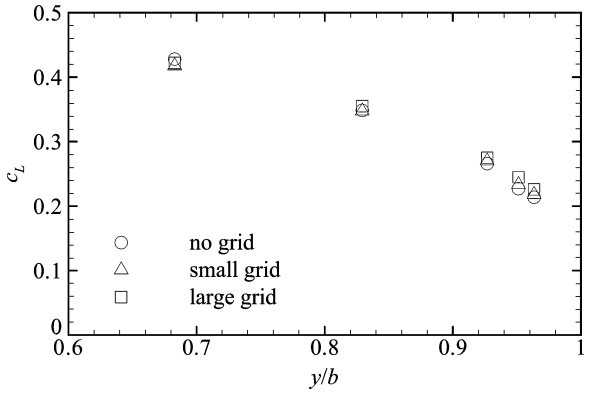

Fig. 9 Variation of section lift coefficients calculated from surface pressure measurements.

trajectories of both vortices A and B were unaffected. However, vortex B appeared to be distorted by interactions with freestream eddies. Moreover, freestream turbulence seemed to increase the turbulence within both vortices, as implied by increased rates of dye diffusion. The influence of freestream turbulence on vortex C can be observed by comparing Fig. 8a for the no-grid case and Fig. 8b for the small-grid case. In the presence of freestream turbulence, vortex C was clearly more turbulent, as evidenced by more rapid dye diffusion.

In summary, the flow visualization and single-sensor hot-wire results demonstrate that freestream turbulence did not introduce any apparent gross change in the vortex formation process, although it affected the initial turbulence level in the vortex core and resulted in increased distortion and meandering of the formation vortices. The negligible effect of freestream turbulence on the loading of the wing and the initial stages of vortex formation is also demonstrated by the fact that the section lift coefficient c_L, determined at $\alpha = 5$ deg in the wind-tunnel experiments by integrating the surface pressure at five spanwise planes, showed a negligible variation with increasing freestream turbulence level (Fig. 9).

Vortex Axis

Time-averaged vortex properties were measured in the wind tunnel by traversing the four-sensor hot-wire probe on several planes normal to the freestream downstream of the wing. Because of wandering, the instantaneous vortex axis was changing location with time and could not be determined precisely with the available instrumentation. Instead, the average location of the intersection of the vortex axis with each measuring plane was identified as the center of a family of concentric circles fitted to isocontours of the magnitude of the time-averaged velocity $(\bar{U}_y^2 + \bar{U}_z^2)^{1/2}$ on the measuring plane. During this process, the orientation of the coordinate system used to calculate the velocity components was adjusted to yield isotachs that were as circular as possible, thus correcting for a possible slight misalignment of the probe axis with respect to the vortex axis. Typically, this required coordinate axis rotations by less than 5 deg. This locus, which may be called the average vortex axis or average vortex trajectory, is shown in Fig. 10, where y_v and z_v are its spanwise and vertical distances from the wing-tip quarter-chord location. It can be seen that, for all three freestream turbulence levels examined, the vortex moved inboard and upward from the tip of the wing. Also apparent from Fig. 10 is that the vortex trajectory was not significantly affected by the introduction of freestream turbulence.

Axial Velocity

The variations of the dimensionless mean streamwise velocity over the measurement plane are presented as contours of $\bar{U}_x/U_0$ for each of the three freestream conditions in Fig. 11 for $x/c = 1.75$, in Fig. 12 for $x/c = 5.75$, and in Fig. 13 for $x/c = 9.75$. The results have been normalized by the local freestream velocity U_0 on the corresponding measuring plane, which was higher by up to 5% than the undisturbed freestream velocity U_∞ because of blockage by the wing and its wake. Measurements at the three streamwise

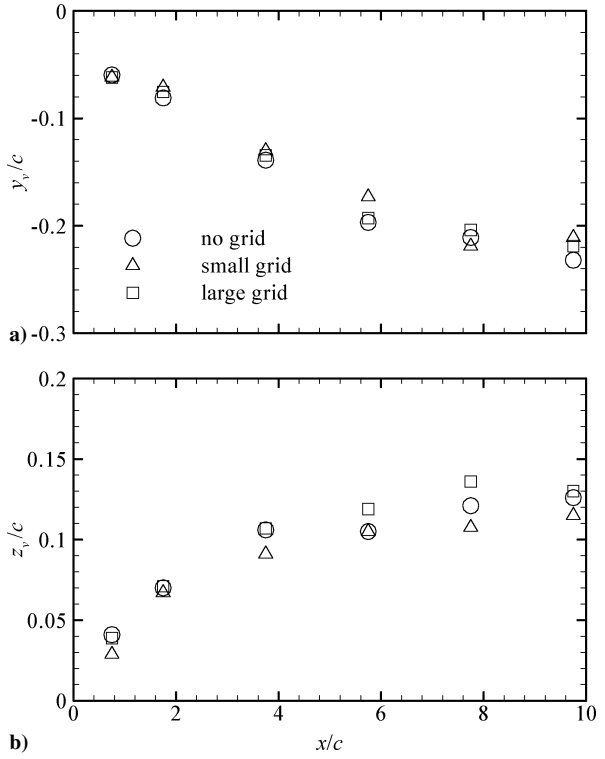

Fig. 10 Distances of vortex axis from streamwise line passing through wing's aerodynamic center: a) spanwise direction and b) direction of lift.

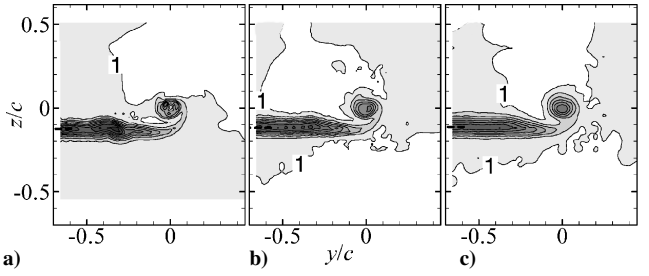

Fig. 11 $\bar{U}_x/U_0$ contours at $x/c = 1.75$: a) no-grid, b) small-grid, and c) large-grid cases.

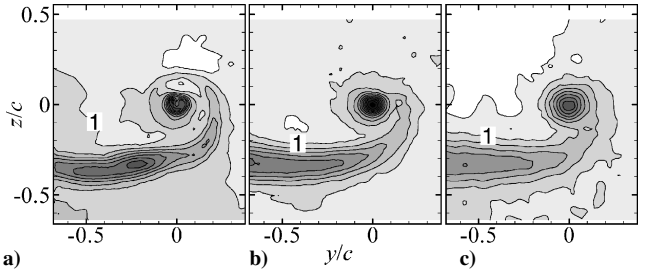

Fig. 12 $\bar{U}_x/U_0$ contours at $x/c = 5.75$: a) no-grid, b) small-grid, and c) large-grid cases.

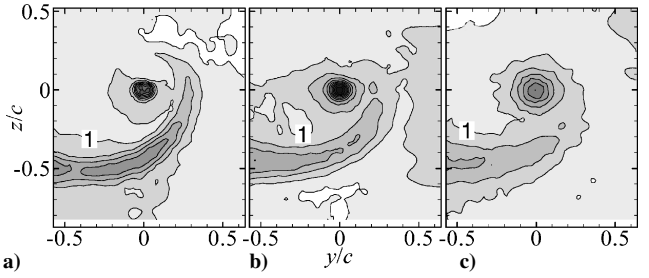

Fig. 13 $\bar{U}_x/U_0$ contours at $x/c = 9.75$: a) no-grid, b) small-grid, and c) large-grid cases.

stations $x/c = 1.75$, 5.75, and 9.75 are used to indicate the trend of streamwise development for each of the three cases.

In Figs. 11–13, the wing wake can be identified as a thin region having a velocity deficit. At $x/c = 1.75$, the isovelocity contours within the wake contain long, relatively straight sections, but contour curvature increases with increasing downstream distance, as the wake spirals around the vortex due to the velocity field induced by the latter. A nearly axisymmetric region of velocity deficit surrounding the vortex axis, is evident in Figs. 11–13. In Fig. 11, contour lines are spaced 0.02 apart, whereas in Figs. 12 and 13 they are 0.01 apart. In Figs. 11–13, lower values are indicated by darker-gray.

Increasing freestream turbulence appeared to increase the rate of diffusion of the streamwise momentum within the spiral wake. This was expressed as both an increase in the wake width and a corresponding decrease in velocity deficit. Moreover, increasing freestream turbulence resulted in a decrease in the curvature of the wake, which may be interpreted as a reduction in the strength of the velocity field induced by the vortex. This reduction in wake curvature is not an artifact of the measuring procedure because it cannot be attributed to vortex meandering.

For a closer examination of the axial velocity variation near the vortex axis, the radial variations of the dimensionless mean streamwise velocity $\bar{U}_x/U_0$ for each of the three freestream conditions are shown in Figs. 14–16. For clarity, measurements within the spiral wake are indicated by solid squares, so that they can be distinguished from measurements in the freestream.

An issue of interest is to determine whether, for the different freestream conditions, the time-averaged streamwise velocity in the vortex core is jetlike or wakelike, namely, whether the peak streamwise velocity $\bar{U}_p$ in the core is greater or smaller than U_0 (Refs. 7, 8, and 10). The measurements in the no-grid case at $x/c = 1.75$ (Fig. 14a) appear to conform with neither of these patterns. Instead, the axial velocity profile has a local maximum at the vortex center, roughly equal to the local freestream velocity, surrounded by an annular region with a velocity deficit. As the vortex develops downstream, both the central maximum and the annular deficit decrease and the axial velocity profile approaches a wakelike form. Considering that lateral vortex motion would generally tend to smoothen the time-averaged velocity profile, one may not assert the degree, if any, by which the observed changes in the mean profile are caused

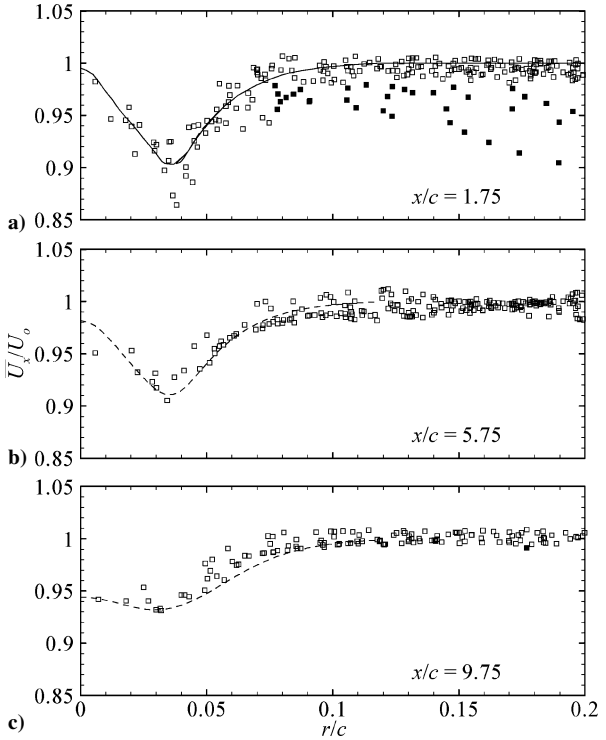

Fig. 14 Radial variation of measured normalized mean axial velocity for no-grid case: a) $x/c = 1.75$, b) $x/c = 5.75$, and c) $x/c = 9.75$.

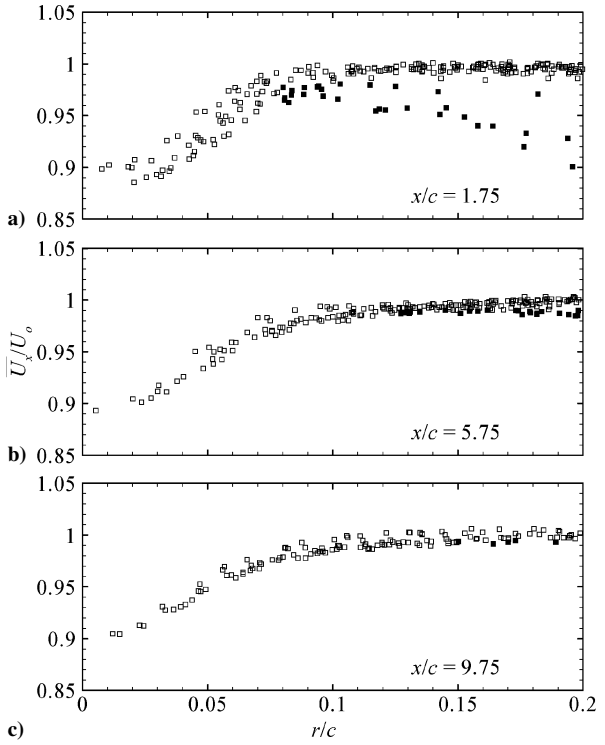

Fig. 15 Radial variation of mean streamwise velocity normalized by local freestream velocity $\bar{U}_x/U_0$, small-grid case: a) $x/c = 1.75$, b) $x/c = 5.75$, and c) $x/c = 9.75$: ■, data points in spiral wake.

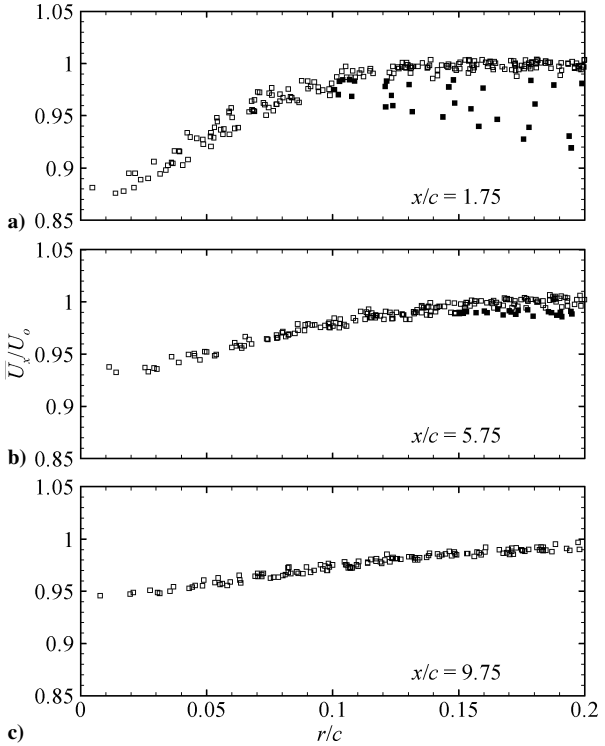

Fig. 16 Radial variation of mean streamwise velocity normalized by local freestream velocity $\bar{U}_x/U_0$, large-grid case: a) $x/c = 1.75$, b) $x/c = 5.75$, and c) $x/c = 9.75$: ■, data points in spiral wake.

by vortex wandering or whether they are the result of changes in the instantaneous profiles.

To illuminate this issue, a simple model was created by introducing a random transverse motion of the velocity profile indicated by a solid line in Fig. 14a, which is an approximation of the measured mean profile. Two time series representing the instantaneous displacements in the y and z directions of the vortex axis from the fixed origin with zero means and standard deviations σ_y and σ_z, respectively, were generated using a Gaussian random number generator. A series of points along a radial line was chosen to represent locations of the fixed measuring probe, and a time series of the velocity U_x at each point was formed by selecting appropriate values from the velocity profile of the randomly moving vortex. Mean values $\bar{U}_x$ were calculated from the series for different values of $\sigma_y = \sigma_z = \sigma$, which correspond to the amplitudes of wandering motion. The results for $\sigma = 0.005c$ (=1 mm) and $\sigma = 0.017c$ (=3 mm) are presented in Figs. 14b and 14c respectively, as dashed lines. Despite its crudeness, this model reproduces fairly well the profiles measured at $x/c = 5.75$ and 9.75 for the no-grid case. In other words, the shapes of the mean profiles measured downstream are approximately the same as the mean profiles that would be observed by a fixed probe, if a vortex with a fixed instantaneous profile equal to the mean profile at $x/c = 1.75$ were set in Gaussian-type vortex wandering. Note that the rms amplitudes of wandering estimated at each location are actually conservative because they are based on the assumption that the profile at $x/c = 1.75$ is not itself subjected to wandering. However, these values are significantly larger than predicted using the correction technique of Devenport et al.,[8] which implies either the correction is inaccurate or the streamwise development shown in Fig. 14 is due to effects other than vortex wandering. Because of the agreement of the experimental results of Heyes et al.[20] with the technique of Devenport et al.,[8] it appears more likely that the development is due to effects other than vortex wandering. For the turbulent freestream cases, for which vortex wandering would be much stronger than that in the no-grid case, one would anticipate that instantaneous radial profiles of the streamwise velocity could be even more different in shape from the mean profiles measured by a fixed probe.

The measured profiles of $\bar{U}_x/U_0$ are presented for the small-grid case in Fig. 15 and the large-grid case in Fig. 16. In both cases, the velocity distributions appear wakelike. Both profiles were clearly asymmetric near the vortex axis at $x/c = 1.75$, but their asymmetry decreased with increasing downstream distance. Whereas the profiles in the small-grid case show very little change in magnitude and radial scale as the downstream distance increases, those in the large-grid case show a decreasing deficit and an increasing radial scale.

It is clear that vortex wandering caused by freestream turbulent eddies with sufficiently large size and energy could possibly obscure the measurement of an annular velocity profile by smoothing velocity differences, reducing peak values, and spreading the profile radially, in a process that could be termed as apparent radial diffusion. Thus, differences in the observed profiles for different freestream conditions could be due partly to differences in the instantaneous profiles and partly to differences in wandering effects. This issue remains under investigation and will be revisited in future reports.

Circumferential Velocity

In the present study, the mean circumferential velocity is defined as

$$\bar{U}_\theta = \bar{U}_z \cos\theta - \bar{U}_y \sin\theta \tag{1}$$

where the angle θ is the circumferential coordinate of the probe in a Cartesian coordinate system having the local mean vortex center as origin (Fig. 1). Distributions of $\bar{U}_\theta/U_0$ in the measurement planes are presented as contours for each of the three freestream conditions in Fig. 17 for $x/c = 1.75$, Fig. 18 for $x/c = 5.75$, and Fig. 19 for $x/c = 9.75$. In Figs. 17–19, the locus of minimum $\bar{U}_x/U_0$ in the spiral wake has been indicated by a dashed line and contour lines are spaced 0.02 apart, with the contour level 0.08–0.1 shown in gray.

Near the vortex axis, $\bar{U}_\theta/U_0$ appears to be nearly axisymmetric; however, as r/c increases, the asymmetry in circumferential velocity becomes more pronounced. Near the wing, at $x/c = 1.75$, the outer isotachs resemble a mirrored letter C in shape, whereas farther downstream, the contours evolve to include an arm of increased circumferential velocity in the spiral wake region. This asymmetry is most likely caused by effects of the spanwise velocity induced

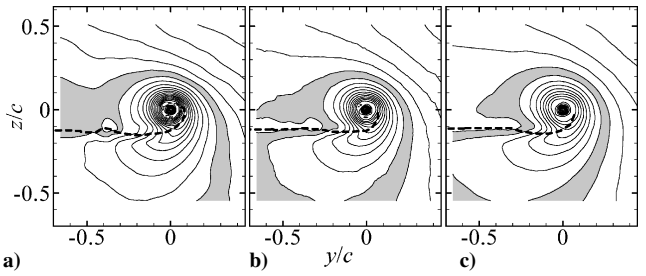

Fig. 17 $\bar{U}_\theta/U_\infty$ contours at $x/c = 1.75$: a) no-grid, b) small-grid, and c) large-grid cases.

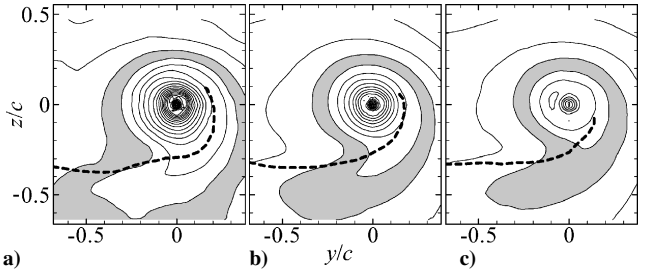

Fig. 18 $\bar{U}_\theta/U_\infty$ contours at $x/c = 5.75$: a) no-grid, b) small-grid, and c) large-grid cases.

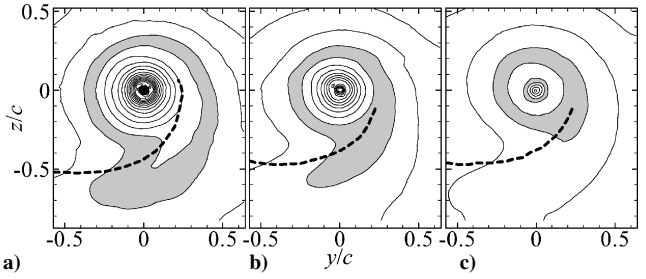

Fig. 19 $\bar{U}_\theta/U_\infty$ contours at $x/c = 9.75$: a) no-grid, b) small-grid, and c) large-grid cases.

over the pressure and suction surfaces of the wing, the residual of which is visible at $x/c = 1.75$. Downstream of the wing, this induced velocity evolves through viscous effects into a shear layer, which appears as the arm of increased $\bar{U}_\theta/U_0$ at $x/c = 5.75$ and 9.75. The shear layer largely coincides with the spiral wake, and they follow the same trajectory, as shown by the dashed lines in Figs. 17–19.

Within the shear layer, isotachs of circumferential velocity across the spiral wake are oriented at an angle to the wake, indicating that the wake is undergoing both stretching and shearing, in agreement with discussion by Miranda and Devenport.[22] For all three freestream conditions, the angles between the velocity contours and the wake trajectory are comparable, which indicates that the relative strengths of stretching and skewing change in proportion with the increase in freestream turbulence. Also apparent in Figs. 17–19 is a decrease in the rates of both stretching and shearing in the wake as freestream turbulence increases. Stretching in the direction of the spiral tends to increase the azimuthal vorticity component, whereas shearing tends to produce additional turbulence in the wake. Because these effects appear to weaken with increasing freestream turbulence, one would expect that the influence of the wake on the vortex would also weaken.

The most likely reason for the reduction in shearing and stretching is the lateral spreading of the shear layer caused by an increase in turbulent diffusion. Such increases in diffusion occur both with increasing streamwise distance and increasing freestream turbulence. Phillips[23] describes the process of shear-layer stretching during rollup, while the innermost spirals merge together through viscous diffusion to form the vortex core. This process, combined with an increased rate of diffusion due to more intense freestream turbulence, provides a mechanism for an increase in the vortex core radius at distances far downstream of the wing, where the vortex rollup is complete.

The axisymmetric region of $\bar{U}_\theta/U_0$ near the vortex axis is illustrated by the radial profiles of $\bar{U}_\theta/U_0$, shown in Figs. 20–22, respectively, for each of the three freestream conditions. The increasing scatter in $\bar{U}_\theta/U_0$ as r/c increases beyond about 0.75 is attributed to the shear layer observed in Figs. 17–19. This scatter diminishes with streamwise distance, which indicates a decrease in the mean shear, as the shear layer becomes integrated into the vortex. To clarify

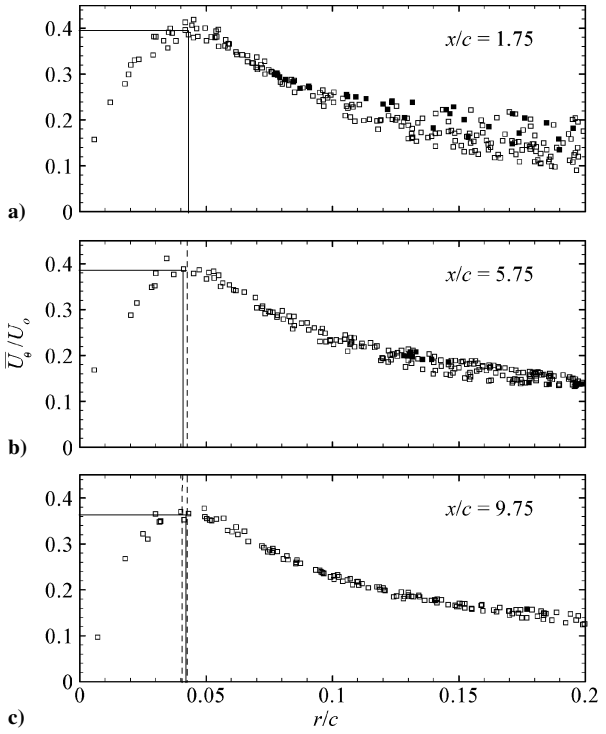

Fig. 20 Mean circumferential velocity, no-grid case: a) $x/c = 1.75$, b) $x/c = 5.75$, and c) $x/c = 9.75$.

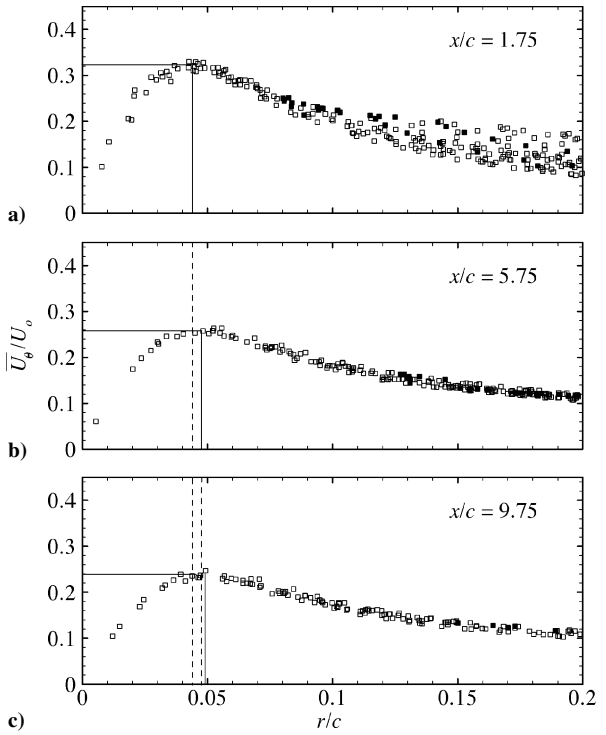

Fig. 21 Mean circumferential velocity, small-grid case: a) $x/c = 1.75$, b) $x/c = 5.75$, and c) $x/c = 9.75$.

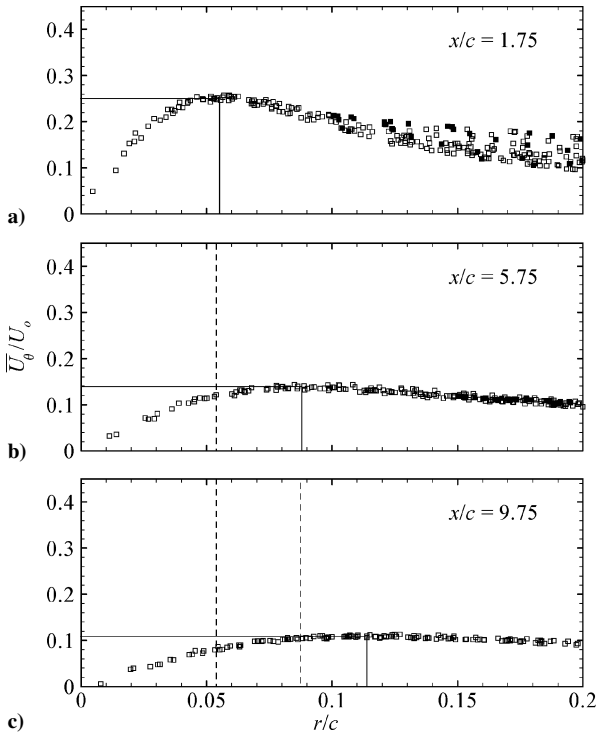

Fig. 22 Mean circumferential velocity, large-grid case: a) $x/c = 1.75$, b) $x/c = 5.75$, and c) $x/c = 9.75$.

the contribution of measurements in the spiral wake to the overall scatter, such measurements have been indicated by solid symbols in Figs. 20–22. All profiles have a distinct peak with a value $\bar{U}_{\theta\,\max}/U_0$, located at a radial distance $r_{\theta\,\max}/c$. Both the peak values and the peak locations have been identified in Figs. 20–22. Other than a decreasing amount of scatter in the data, the no-grid circumferential velocity profile showed little change with streamwise distance (Fig. 20). In contrast, the peak in the small-grid profile decreased measurably and moved to clearly larger radial positions (Fig. 21). The same trends were demonstrated in a much more dramatic way by the large-grid profile (Fig. 22). For comparative purposes, we shall refer to the region encircled within the radius of the peak in the mean circumferential velocity as the apparent vortex core. Correspondingly, the peak amplitude and radial position will be referred to as the apparent core peak velocity and the apparent core radius, respectively.

The circumferential velocity profiles in the apparent cores of wing-tip vortices in nonturbulent freestreams are known to develop in a self-similar fashion, if $\bar{U}_\theta$ and r are normalized by the peak value $\bar{U}_{\theta\,\max}$ and the peak radius $r_{\theta\,\max}$, respectively.[23] Figure 23 shows that this applies not only to the present no-grid profile but also to the profiles for both cases of grid turbulence. In all cases, collapse of the data was fairly consistent within the range $r/r_{\theta\,\max} < 1.2$, but the scatter increased with increasing dimensionless radius outside that range. Moreover, the data within the apparent vortex core were described fairly well by the curve fit proposed by Phillips,[23] who also noted that, for $r/r_{\theta\,\max} \gtrapprox 1.2$, the circumferential velocity profile would not be self-similar, but its shape would depend on the conditions occurring during vortex formation. Note that the mean velocity profiles for the turbulent freestreams develop in self-similar fashions, despite the fact that they are strongly influenced by vortex meandering and could, therefore, be quite different from the corresponding instantaneous velocity profiles. It is not clear whether this would be the case if the freestream had an arbitrary turbulence structure because grid turbulence also develops self-similarly.

The changes of the apparent core parameters $\bar{U}_{\theta\,\max}/U_0$ and $r_{\theta\,\max}/c$ with streamwise distance for the three freestream conditions are shown in Figs. 24a and 24b. In the no-grid case, these parameters changed very slightly, if at all, which indicates that the corresponding profiles were essentially free of wandering effects. As mentioned earlier, freestream turbulence resulted in an apparent

Table 1 Power law coefficients

Case	a	m	d	n
Small grid	0.35	0.2	0.04	0.1
Large grid	0.32	0.5	0.04	0.4

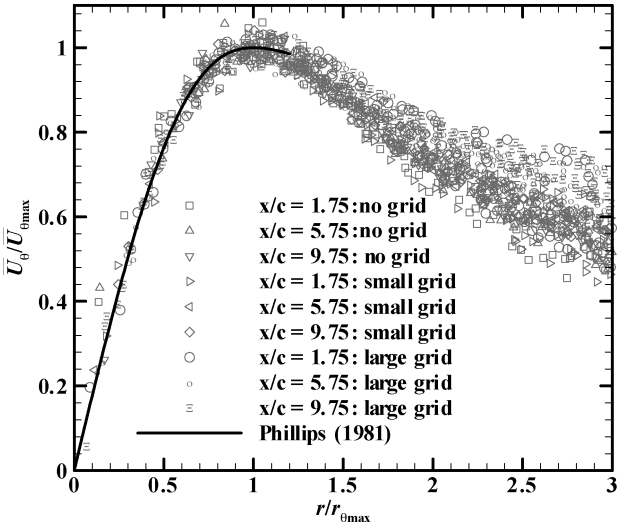

Fig. 23 Radial profiles of the mean circumferential velocity in normalized axes: ——, self-similar curve proposed by Phillips.[23]

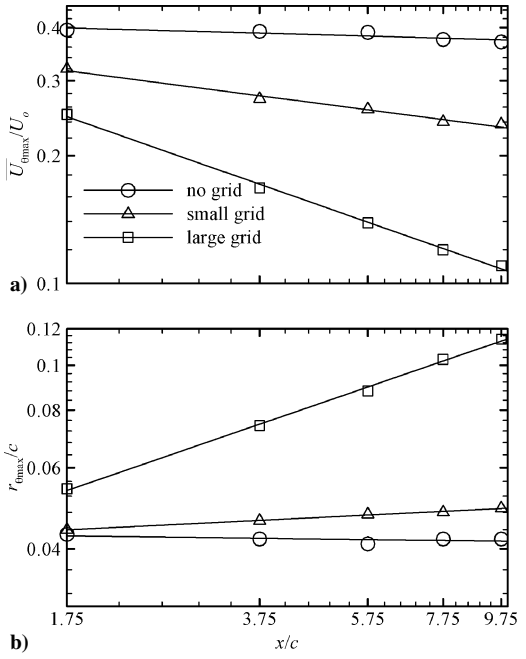

Fig. 24 Streamwise development of a) $\bar{U}_{\theta\,\max}/U_0$ and b) $r_{\theta\,\max}/c$: ——, fitted power law.

diffusion of these profiles, causing $\bar{U}_{\theta\,\max}$ to decay and $r_{\theta\,\max}$ to grow, with both effects intensified with increasing freestream turbulence. The changes of both parameters with streamwise distance could be well represented by fitted power laws as

$$\bar{U}_{\theta\,\max}/U_0 = a(x/c)^{-m} \tag{2}$$

$$r_{\theta\,\max}/c = d(x/c)^{n} \tag{3}$$

with the coefficients and exponents summarized in Table 1.

Like the radial profiles of the mean axial velocity, measured radial profiles of the mean circumferential velocity are subjected to the effects of vortex wandering, which is expected to become stronger with increasing freestream turbulence. This can be further illustrated

by considering the change in the angular momentum of the fluid contained in the apparent core. Away from the origin, there is no source of external torque that would increase this angular momentum, so one would expect that, if the measured value represented well the corresponding value in the wandering vortex, it would have to remain constant, or most likely decrease due to viscous actions. The apparent core angular momentum, estimated using the fit of Phillips,[23] was found to be proportional to $r_{\theta\,\max}^3 \bar{U}_{\theta\,\max}$. Thus, it increased as $(x/c)^{0.1}$ for the small-grid case and as $(x/c)^{0.7}$ for the large-grid case. These results clearly demonstrate an increasing influence of vortex meandering on the circumferential velocity profiles. At the same time, freestream turbulence may also alter the actual structure of the vortex, diffusing its core faster and affecting the instantaneous profiles. A recent experimental study by Heyes et al.,[20] using particle image velocimetry to determine instantaneous profiles under conditions comparable to those of the present small-grid case, attributed the apparent diffusion of the vortex almost entirely to turbulence-induced lateral motion. Present results, most notably those in the large-grid case in which freestream turbulence was much stronger than that in the Heyes et al. experiments, contradict this conclusion. The rapid rate of growth of the apparent core and the reduced curvature of the spiral wake hint that at least some of the apparent diffusion could be due to diffusion of the vortex circulation.

Conclusions

An experimental investigation of the influence of freestream turbulence on a wing-tip vortex was conducted for a rectangular-planform, square-tip wing with a NACA 0012 profile. Three turbulence levels were examined consisting of a low-turbulence freestream and two grid turbulence cases. The wing-tip vortex was found to form from three distinct corotating vortices whose positions were unaffected by freestream turbulence, although flow visualization indicated an increase in turbulence within these vortices. Freestream turbulence also did not seem to introduce any measurable change in the mean trajectory of the vortex; however, it reduced the mean curvature of the wing wake axis, pointing to a possible reduction of vortex strength. The mean axial velocity profile had an annular shape in the no-grid case close to the wing and developed toward a wakelike shape with increasing streamwise distance. Both grid cases had wakelike mean axial profiles, which were found to be affected significantly by vortex meandering. The shear layer shed from the wing was found to both stretch and shear the wing wake. Increased freestream turbulence resulted in reduced stretching and shearing, although the relative strengths of stretching and shearing remained in proportion. Circumferential velocity profiles near the mean vortex axis were also found to be strongly affected by vortex meandering with increased freestream turbulence resulting in increased meandering. For all cases, the circumferential velocity profiles in the apparent cores were found to be self-similar, despite meandering.

Acknowledgments

Financial support was provided by Natural Sciences and Engineering Research Council of Canada. The four-sensor probe was provided by Petar Vukoslavčević. Petar Vukoslavčević and Metin Yaras are gratefully acknowledged for their assistance in the early stages of this work.

References

[1]Spalart, P., "Airplane Trailing Vortices," *Annual Review of Fluid Mechanics*, Vol. 30, 1998, pp. 107–138.

[2]Katz, J., and Galdo, J., "Effect of Roughness on Rollup of Tip Vortices on a Rectangular Hydrofoil," *Journal of Aircraft*, Vol. 26, No. 3, 1989, pp. 247–253.

[3]Birch, D., Lee, T., Mokhtarian, F., and Kafyeke, F., "Rollup and Near-Field Behavior of a Tip Vortex," *Journal of Aircraft*, Vol. 40, No. 3, 2003, pp. 603–607.

[4]Jacquin, L., Fabre, D., Geffroy, P., and Coustols, E., "The Properties of a Transport Aircraft Wake in the Extended Near Field: An Experimental Study," AIAA Paper 2001-1038, Jan. 2001.

[5]Cotel, A., and Breidenthal, R., "Turbulence Inside a Vortex," *Physics of Fluids*, Vol. 11, No. 10, 1999, pp. 3026–3029.

[6]Bradshaw, P., "The Analogy Between Streamline Curvature and Buoyancy in Turbulent Shear Flow," *Journal of Fluid Mechanics*, Vol. 36, 1969, pp. 177–191.

[7]Chow, J., Zilliac, G., and Bradshaw, P., "Mean and Turbulence Measurements in the Near Field of a Wingtip Vortex," *AIAA Journal*, Vol. 35, No. 10, 1997, pp. 1561–1567.

[8]Devenport, W., Rife, M., Stergios, I., and Follin, G., "The Structure and Development of a Wing-Tip Vortex," *Journal of Fluid Mechanics*, Vol. 312, 1996, pp. 67–106.

[9]Batchelor, G., "Axial Flow in Trailing Line Vortices," *Journal of Fluid Mechanics*, Vol. 20, 1964, pp. 645–658.

[10]Anderson, E., and Lawton, T., "Correlation Between Vortex Strength and Axial Velocity in a Trailing Vortex," *Journal of Aircraft*, Vol. 40, No. 4, 2003, pp. 699–704.

[11]Singh, P., and Uberoi, M., "Experiments on Vortex Stability," *Physics of Fluids*, Vol. 19, No. 12, 1976, pp. 1858–1863.

[12]Marshall, J., and Beninati, M., "Turbulence Evolution in Vortex-Dominated Flows," *Nonlinear Instability, Chaos and Turbulence II*, WIT Press, Southampton, England, U.K., 2000, pp. 1–40.

[13]Baker, G., Barker, S., Bofah, K., and Saffman, P., "Laser Anemometer Measurements of Trailing Vortices in Water," *Journal of Fluid Mechanics*, Vol. 65, 1974, pp. 325–336.

[14]Bandyopadhyay, P., Stead, D., and Ash, R., "Organized Nature of a Turbulent Trailing Vortex," *AIAA Journal*, Vol. 29, No. 10, 1991, pp. 1627–1633.

[15]Holzäpfel, F., Hofbauer, T., Darracq, D., Moet, H., Garnier, F., and Gago, C., "Analysis of Wake Vortex Decay Mechanisms in the Atmosphere," *Aerospace Science and Technology*, Vol. 7, No. 4, 2003, pp. 263–275.

[16]Beninati, M., and Marshall, J., "An Experimental Study of the Effect of Free-Stream Turbulence on a Trailing Vortex," *Experiments in Fluids*, Vol. 38, No. 2, 2005, pp. 244–257.

[17]Wittmer, K., Devenport, W., and Zsoldos, J., "A Four-Sensor Hot-Wire Probe System for Three-Component Velocity Measurements," *Experiments in Fluids*, Vol. 24, No. 5-6, 1998, pp. 416–423.

[18]Döbbeling, K., Lenze, B., and Leuckel, W., "Basic Considerations Concerning the Construction and Usage of Multiple Hot-Wire Probes for Highly Turbulent Three-Dimensional Flows," *Measurement Science and Technology*, Vol. 1, No. 9, 1990, pp. 924–933.

[19]Rae, W. H., and Pope, A., *Low Speed Wind Tunnel Testing,* 2nd ed., Wiley, New York, 1984, Chap. 6, pp. 344–444.

[20]Heyes, A., Jones, R., and Smith, D., "Wandering of Wing-Tip Vortices," *Proceedings of the 12th International Symposium on the Applications of Laser Techniques to Fluid Mechanics*, Calouste Gulbenkian Foundation, Paper No. 35-3, Lisbon, July 2004, p. 20.

[21]McInerny, S., Meecham, W., and Soderman, P., "Pressure Fluctuations in the Tip Region of a Blunt-Tipped Airfoil," *AIAA Journal*, Vol. 28, No. 1, 1990, pp. 6–13.

[22]Miranda, J., and Devenport, W., "Turbulence Structure in the Spiral Wake Shed by a Lifting Wing," *AIAA Journal*, Vol. 36, No. 4, 1998, pp. 658–660.

[23]Phillips, W., "The Turbulent Trailing Vortex During Roll-Up," *Journal of Fluid Mechanics*, Vol. 105, 1981, pp. 451–467.